X-band epi-BAW resonators

View Online   Export Citation   CrossMark

Wenwen Zhao,[1,a)] Mohammad Javad Asadi,[2] Lei Li,[2] Reet Chaudhuri,[2] Kazuki Nomoto,[2]
Huili Grace Xing,[2,3,4] James C. M. Hwang,[2,3] and Debdeep Jena[2,3,4,b)]

AFFILIATIONS

[1]School of Applied and Engineering Physics, Cornell University, Ithaca, New York 14853, USA
[2]School of Electrical and Computer Engineering, Cornell University, Ithaca, New York 14853, USA
[3]Department of Materials Science and Engineering, Cornell University, Ithaca, New York 14853, USA
[4]Kavli Institute at Cornell for Nanoscale Science, Ithaca, New York 14853, USA

[a)]Electronic mail: wz344@cornell.edu
[b)]Author to whom correspondence should be addressed: djena@cornell.edu

ABSTRACT

Using epitaxial aluminum nitride (AlN) developed for ultraviolet photonics and high-speed electronics, we demonstrate suspended AlN thin-film bulk acoustic resonators (FBARs) at 9.2 GHz in the X-band (8–12 GHz) of the microwave spectrum. The resonators show a $Q_{max} \approx 614$ and a figure of merit $f \cdot Q \approx 5.6$ THz. The material stack of these epi-AlN FBARs allows monolithic integration with AlN/GaN/ AlN quantum well high-electron-mobility-transistors to a unique RF front end and also enable integration with epitaxial nitride superconductors for microwave filters for quantum computing.

I. INTRODUCTION

Filters are core passive components in communication systems that comprise a rapidly expanding market projected to increase with emerging 5G technology, internet of things, sensors, and automation.[1–3] While surface acoustic wave (SAW) filters dominate for operation below 2 GHz due to simplicity of fabrication, their performance for higher frequencies is limited by a low surface acoustic wave velocity, lithographic complexity, and a low quality factor.[1,4] The electro-migration damage in the narrow interdigital transducer (IDT) fingers and an uneven current distribution of SAW result in the poorer power handling compared to bulk acoustic wave (BAW) filters.[1] BAW filters dominate in the lower 5G bands ranging from 1.5 to 6 GHz because of a higher velocity of thickness-extensional waves than that of the surface acoustic waves. A high quality factor and high power handling enables BAW filters to be scaled to higher frequencies while maintaining high RF performance.[1] The advantages of miniaturization due to such electro-acoustic filtering (since the wavelength of acoustic waves is much smaller than electromagnetic waves for the same frequency) face diminishing returns for higher frequencies in the mm-wave range (30–300 GHz). For such high frequencies, direct filtering in the optical domain using substrate integrated waveguides (SIWs) and cavity filters dominate.[5–9]

Thin-film bulk acoustic resonators (FBARs) are BAWs that utilize a suspended thin-film piezoelectric material as the resonating layer. The FBAR is a metal–insulator–metal (M–I–M) capacitor in which the insulating layer is piezoelectric. The device is an acoustic cavity: the metal electrodes (typically W, Pt, Mo, or Cu that possess high electrical conductivity and high acoustic impedance) transduce the electronic oscillation to mechanical through the piezoelectric effect.[1] The resonance frequency of an acoustic cavity scales inversely with the effective dimension of the resonant cavity. The first-order resonance mode of a cavity of thickness L satisfies $2L = \lambda$ for perfectly reflecting mirrors, where λ is the sound wavelength. The resonance frequency $f = v_s/2L$ of a FBAR increases as the piezoelectric layer is made thinner. Here, v_s is the sound velocity in the piezoelectric layer.

AlN is widely used as the piezoelectric layer of FBARs for its high electromechanical coupling coefficient, high acoustic phase velocity, and low acoustic and dielectric losses as well as compatibility with CMOS process conditions.[10,11] Recently, aluminum scandium nitride (AlScN) alloy has also been explored due to significantly higher electro-mechanical coupling and promise for intrinsic switching due to accessible ferroelectricity.[12–14]

Currently, the AlN resonators in the commercial filters are based on the physical vapor deposited (PVD) films, such as sputtered polycrystalline piezoelectric films. BAW filters with a single

crystal, epitaxially grown AlN offer potential performance advantages over their polycrystalline counterparts because of improved acoustic velocity, piezoelectric coefficient, and power handling.[15–17] Single crystalline AlN grown by metalorganic chemical vapor deposition (MOCVD) or molecular-beam epitaxy (MBE) provide a way to realize high frequency (>6 GHz) acoustic filters with a high quality factor and high power handling.[15–22]

In addition to being an excellent piezoelectric, highly crystalline AlN is also a wide-bandgap semiconductor used in UV photonics and RF transistor amplifiers. An exciting opportunity enabled by single crystalline BAW filters is the monolithic integration of passive filters with active devices, such as high-electron-mobility-transistor (HEMT) amplifiers. While BAWs can be fabricated by sputtering, nitride transistor amplifiers require epitaxial growth. Several groups have demonstrated active filtering based on the GaN acoustic resonators and HEMTs.[23–25] Based on SiC substrates with high thermal conductivity and mechanical toughness, the convergence of AlN FBAR and AlN HEMT material layers by epitaxy can enable a unique RF front end. AlN/GaN/AlN quantum well HEMTs with a record on-current of 3.6 A/mm and a record maximum oscillation frequency (f_{max}) of 233 GHz were recently demonstrated.[26] In such HEMTs, the conventional AlGaN barrier layer and the AlGaN back barrier layer are replaced with unstrained AlN epitaxial layers. AlN allows for a smarter, highly scaled heterostructure design that improves the output power and thermal management of III-nitride semiconductor amplifiers.[27,28] Figure 1 shows a scheme for the monolithic integration of an AlN FBAR filter and an AlN/GaN/AlN quantum well HEMT on an SiC substrate. By utilizing the AlN buffer layer of the HEMT, FBARs can be fabricated on the same SiC substrate by fully suspending the piezoelectric cavity for a higher quality factor using deep through-SiC-vias (TSVs). The monolithic integration can "filter and amplify" with appropriate interconnects, forming a unique "BAWFET" front end.
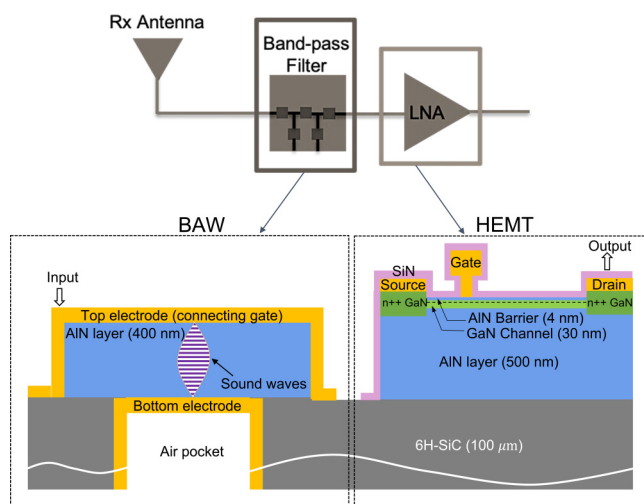
FIG. 1. Schematic of a "BAWFET," with an AlN FBAR and a AlN/GaN/AlN quantum well HEMT on the same 6H-SiC chip.

The HEMT portion in Fig. 1 was recently reported in Refs. 26 and 27. This work focuses on the design, fabrication, and analysis of AlN-on-SiC FBARs using the same epitaxial process to demonstrate resonators operating at the first-order thickness-extensional mode of $f = 9.2$ GHz. For the 9.2-GHz FBARs in this work, the promising numbers of a maximum loaded quality factor $Q_{max} \approx 614$, $Q_s \approx 540$, $Q_p \approx 439$, $f \cdot Q_{max} = 5.6$ THz, $R_s \approx 25\,\Omega$ (resistance at series resonance), and $R_p \approx 800\,\Omega$ (resistance at parallel resonance) indicate the potential for monolithic integration with RF amplifiers for X-band operations. In the closest related work in Ref. 18, MOCVD grown epi-AlN FBARs operating around a first-order thickness-extensional mode of 12 GHz were reported with $Q_{max} \approx 250$, $f \cdot Q_{max} = 3.1$ THz, and Q_s and Q_p (quality factors at series resonance and parallel resonance) <70, which indicates that the integrated BAW and HEMT can aim for higher frequencies in the near future.

II. EPITAXIAL GROWTH AND CHARACTERIZATION OF AlN ON 6H-SiC

The AlN in this work was grown in a Veeco Gen10 plasma-assisted molecular-beam epitaxy (MBE) system. 6H-SiC is a preferred substrate platform used for RF and mm-wave GaN and AlN-based HEMTs due to its excellent thermal conductivity, hexagonal symmetry, and a close lattice constant to AlN.[27] A 420 nm thick AlN layer was grown on a 3 inch, $100\,\mu m$ thick semi-insulating 6H-SiC wafer on the Si-face side. Growth on the Si-face locks the AlN crystal structure to Al-polarity, as opposed to the chemically more reactive N-polarity achieved on the C-face of SiC. The growth was performed under the following conditions: an Al beam equivalent pressure (BEP) flux of 3.1×10^{-7} Torr at Al/N ratio ≈ 1.05, an RF power of 400 W, an N_2 flow rate of 1.85 sccm, and a substrate temperature of $900\,°C$. The resulting epitaxial AlN growth rate was 6.3 nm/min. As shown in the inset of Fig. 2(a), the sample comprises a 420 nm thick epi-AlN layer (blue) on $100\,\mu m$ thick semi-insulating 6H-SiC (gray).

Because AlN is a direct bandgap semiconductor, a sensitive probe of its structural and chemical quality is photoluminescence (PL) emission. Typically sputtered AlN does not exhibit PL due to non-radiative recombination of electrons and holes at various structural and chemical defects. A PL emission test was performed for the epitaxial AlN on SiC using a pulsed excimer laser ($\lambda = 193$ nm, 2 mJ per pulse, 100 ns pulse width, repetition frequency = 100 Hz) at room temperature. As shown in Fig. 2(a), the AlN layer shows a peak PL emission at 207 nm (≈ 6 eV bandgap), which is absent in the bare SiC substrate. The AlN 002 film peak with a 0.077° full width at half maximum (FWHM) rocking curve was measured by x-ray diffraction (XRD), as shown in Fig. 2(b). The corresponding atomic force microscope (AFM) image shown in Fig. 2(c) indicates a highly smooth surface morphology, with an rms roughness of 0.324 nm for a $10 \times 10\,\mu m^2$ scan of the 420 nm AlN layer. These values indicate high quality epitaxial AlN films.
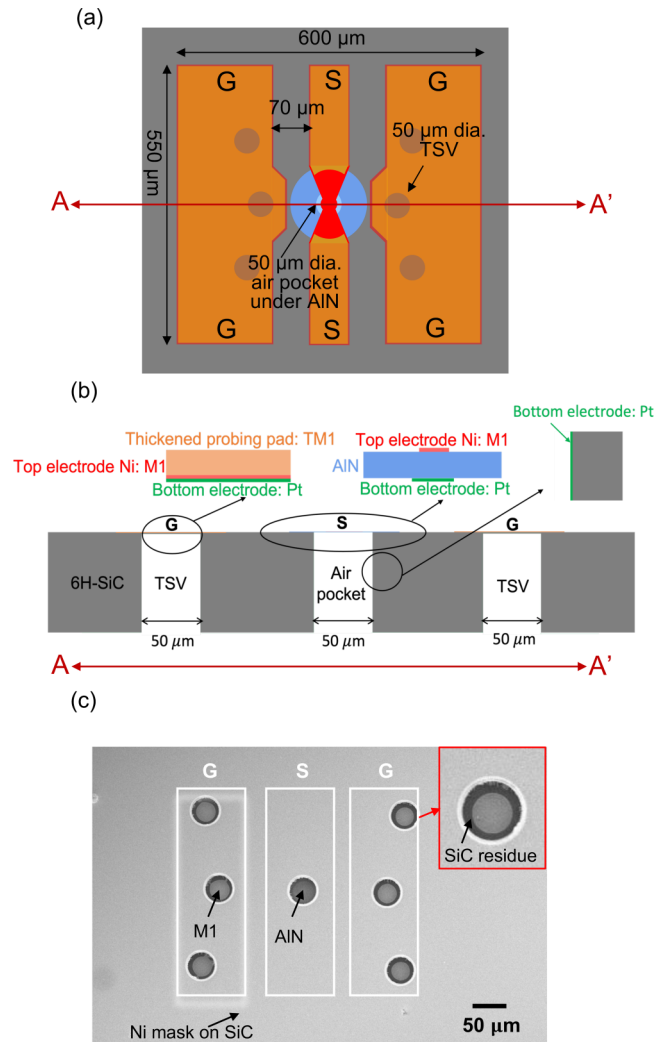
III. DESIGN, FABRICATION, AND ANALYSIS OF EPI-AlN FBARs

If the electrodes are neglected, the resonance frequency of the FBAR is $f = v_s/2L$ with $L \approx \lambda/2$ for the first thickness extension mode. For AlN, using $v_s = 12\,000$ m/s and $L = 420$ nm, the
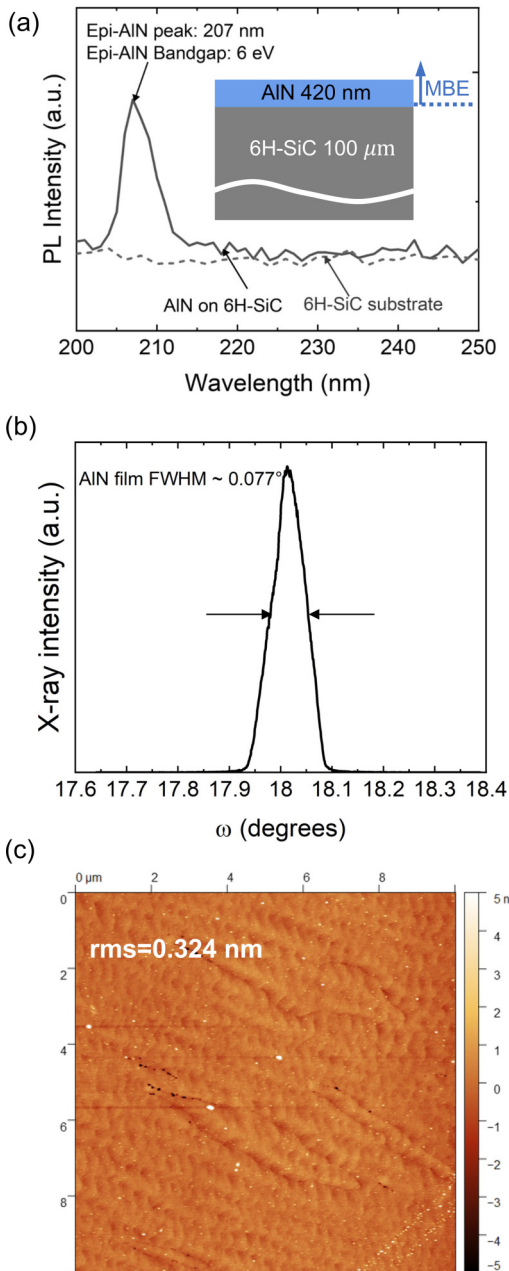
FIG. 2. (a) Photoluminescence spectra for the MBE-grown AlN layer on the 6H-SiC substrate (excitation laser wavelength: 193 nm) showing a near bandgap peak of ≈6.0 eV. (b) AlN 002 film peak rocking-curve XRD scan. (c) 10 × 10 μm^2 AFM scan on the AlN surface.

FIG. 3. (a) Top view and (b) a cross-sectional view of the designed shunt AlN FBAR. FBAR comprises an MBE-grown AlN layer (blue) on semi-insulating 6H-SiC, a top electrode (red), and a backside electrode (green). (c) SEM figure on the SiC's carbon face after deep SiC etching.

resonance frequency expected is $f = 14.3\,GHz$. The penetration of the acoustic wave into the electrodes will lead to a lower resonance frequency; a thin electrode with a low mass density is thus needed to reduce the mass loading on the electromechanically oscillating

layer and to enable high resonance frequencies. A more accurate design of the device geometry for a specific resonance frequency requires numerical simulations, which are discussed next.

Figures 3(a) and 3(b) show a two-port shunt AlN FBAR designed using constitutive equations[1,10,29–31] and finite-element simulators (COMSOL for the piezoelectric effect and HFSS for the effect of the interconnects) and optimized for a first-order thickness-extensional mode around 10 GHz. As shown in the cross-sectional schematic in Fig. 3(b), the FBAR consists of a 420 nm thick MBE-grown AlN layer (blue) on a 100 μm thick semi-insulating SiC substrate (gray), a 50 nm thick top electrode of Ni (red), and a 20 nm thick bottom electrode of Pt (green). There are two types of through-SiC-vias in the design: (1) the air pockets

under the AlN film and (2) the TSVs under the ground lines. Air pockets suspend the electromechanical oscillating AlN layer. The low energy leakage into the substrate in the suspended structure enables a higher quality factor than that of the FBAR mounted on the substrate. TSVs connect the bottom electrode with topside ground lines. Taking quantitative results from the recently demonstrated SiC SIW design parameters,[32] circular TSVs under the ground lines are designed to be 50 μm in diameter. Air pockets are designed to have the same size and shape as the TSVs to eliminate the loading effect during SiC deep etching.

Since the processing steps involve certain complications, we describe them in sufficient detail. The fabrication starts from a quarter 3 in. AlN-on-SiC wafer. A 5-mask layer, two-sided wafer process, including an E-beam evaporated top electrode metal, a deep inductively coupled plasma reactive ion etching (ICP-RIE) on an SiC substrate and a follow-up atomic layer deposited (ALD) bottom electrode metal yielded an epi-AlN FBAR. To better confine the acoustic waves in the piezoelectric layer, Mo or W is usually used as FBAR electrodes. A good etch-stop layer is needed for realizing the TSV. Ni was chosen as the first metal layer (M1) on the top side of the wafer for its high etch-selectivity over SiC, as shown in Figs. 3(a) and 3(b). As Fig. 3(b) indicates, M1 on the ground lines is used as the TSV etch-stop layer, while M1 on the AlN layer is used as the top electrode of FBAR.

The SiC deep etching was performed in an Oxford Cobra ICP-RIE tool at 10 mTorr vacuum, 2000 W ICP power, and 50 W RIE power at a 110 V DC bias with a gas flow of 50 sccm SF_6 and 10 sccm O_2. A 3 μm thick Ni layer was used as the etch mask. The etch rate of SiC is $\approx$15 μm/h. The Ni layer (M1) serves as the etch-stop of the TSV under the ground lines. AlN serves as the etch-stop for the air pockets. In an SF_6/O_2 environment, the etch-selectivity of SiC over AlN is 70 and that of SiC over Ni is 50. An extra metal layer (TM1) of 50 nm Ni and 500 nm Al on the ground lines is used to mitigate TSV over-etching. The etch-stop at Ni makes sure that metallized TSVs connect the bottom electrode with the ground lines on top of the wafer. The etch-stop at AlN indicates a suspended piezoelectric layer. Both etch stops at AlN and Ni layer were carefully controlled using a scanning electron microscope (SEM) and Raman spectroscopy. Figure 3(c) shows an SEM image on the carbon face of SiC after etching. Exposed Ni (M1) exhibits lighter color compared to SiC in Fig. 3(c) due to its higher electrical conductivity.

Since the color contrast between the exposed AlN and SiC is not sharp, Raman spectroscopy was used to confirm if the SiC etch stopped at AlN. Figure 4(a) shows an optical microscope image of the air pocket used for Raman spectroscopy. Figure 4(b) shows the cross-sectional SEM image of the air pocket. As shown in Fig. 4(c), Raman spectra taken by laser excitation through the air pocket shows the characteristic[33] Raman-active phonon vibration mode E_2^H of AlN at $\approx$660 cm^{-1}, confirming a successful TSV formation and that the 420 nm thick AlN layer was suspended from the 100 μm thick SiC after the deep ICP-RIE SiC etching.

Figure 5(a) shows the top view of a fabricated AlN FBAR in shunt configuration. Figure 5(b) is an enlarged SEM image of the active region, in which electromechanical oscillations occur. The top electrode (M1) is E-beam evaporated 50 nm thick Ni. The thickened probing pad (TM1) consisting of 50 nm thick Ni and
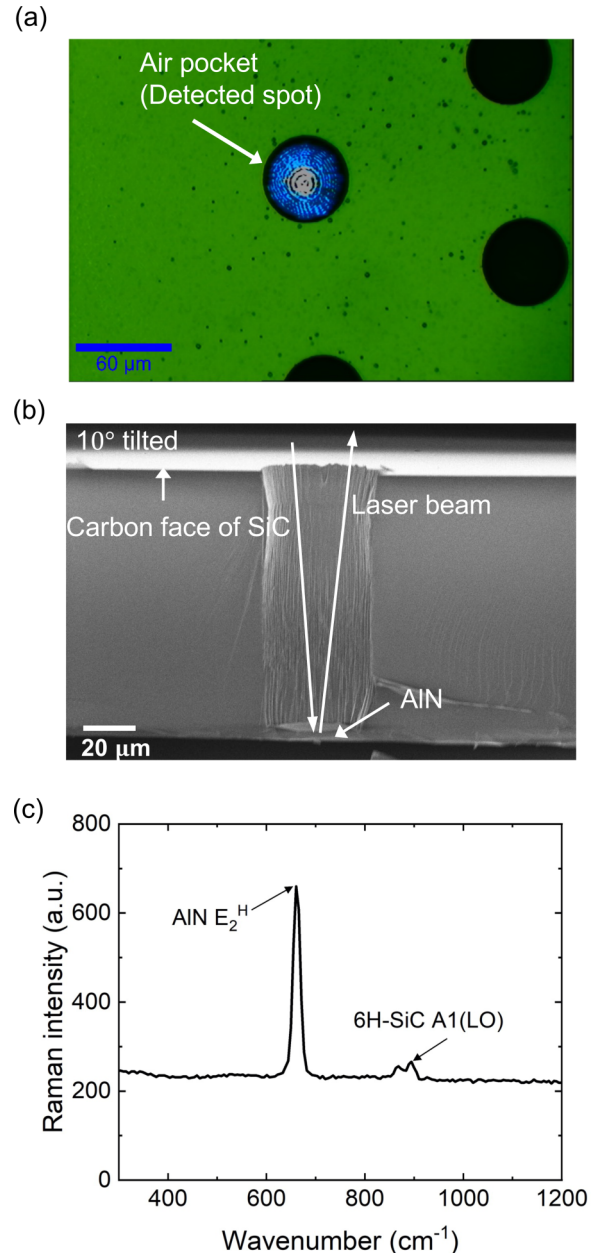
FIG. 4. (a) Optical microscope image of the air pocket for Raman spectroscopy. (b) Cross-sectional SEM figure of an air pocket. (c) Raman spectra for the MBE-grown AlN layer on the 6H-SiC substrate (excitation laser wavelength: 488 nm).

500 nm thick Al was deposited on M1 (except for the region on AlN) to eliminate metal punch-through during SiC etching. The bottom electrode is 20 nm thick ALD Pt. Figure 5(c) shows the suspended metal–AlN–metal layer cross section after backside SiC etching and a bottom electrode deposition.
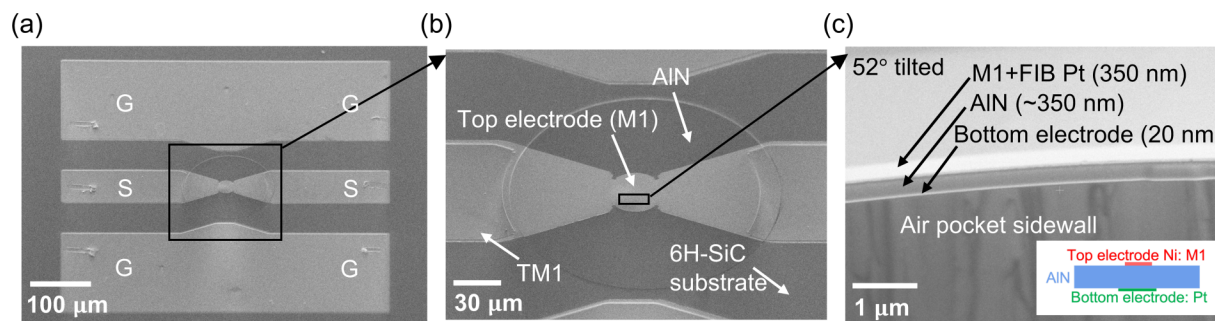
FIG. 5. (a) 45° tilted SEM figure of the fabricated shunt FBAR with 420-nm thick AlN, 50-nm thick Ni as a top electrode and 20-nm thick ALD Pt as a bottom electrode. (b) Enlarged SEM figure of the device vibrating region, including the AlN layer, a top electrode (M1), thickened metal pad (TM1), and the 6H-SiC substrate. (c) 52° tilted cross-sectional SEM figure showing the suspending M–I–M structure after a focused ion beam (FIB) cut.

DC measurements were performed on the AlN FBARs to confirm the electrical conductivity of the metallized TSVs. The measured DC resistance of a TSV with 20 nm thick ALD Pt is 6 Ω per TSV. Based on the known resistivity of Pt, $R = \rho l / A$ is expected to be 3.4 Ω. Here, $l \approx 100 \, \mu m$ is the length of TSV. A is the cross-sectional area of a hollow TSV. The discrepancy may be from the resistive seed layer of Al_2O_3 in an ALD process. FBARs with a lower TSV resistance (<1 Ω) exhibit lower resistive losses and higher quality factors. ALD metals with higher electrical conductivity, such as Al and Ru, will be explored in the future to lower the TSV resistance and improve the quality factors of FBARs.

FBARs with electrically conductive TSVs allow for reliable RF characterization. For RF measurements performed using an Agilent 40-GHz 8722ES vector network analyzer (VNA), the VNA system was calibrated via a short-open-load-through (SOLT) method using an impedance standard substrate. After the VNA calibration, the reference plane was moved to the probes. The on-SiC-wafer open and short devices were used to de-embed the raw data of FBARs, after which the reference plane was moved to the active region of FBARs. However, the metallized air pockets underneath the AlN film are not de-embedded. The quality factors calculated in Fig. 6 are the loaded values. As shown in Figs. 6(a) and 6(b), a series resonance at $f_s \approx 9.17$ GHz and a parallel resonance at $f_p \approx 9.23$ GHz were observed for the fabricated two-port shunt AlN FBAR. The quality factors Q at series resonance and parallel resonance were measured to be 540 and 439, respectively. As shown in Fig. 6(c), a loaded quality factor Q_L for the two-port shunt AlN FBAR driven by a 50-Ω source was extracted using the magnitude and group delay of S_{11}. The frequency dependent Q_L is given by[10] $Q_L(\omega) = 2\pi f \cdot (-d\phi/d\omega) \cdot |S_{11}|/(1 - |S_{11}|^2)$, where ϕ is the phase of S_{11} at f. It is noted that the maximum loaded quality factor Q_{max} is between series and parallel resonance frequencies. Q_{max} plays an important role in determining the insertion loss when the FBAR is employed in a bandpass filter.[34] For the loaded two-port shunt AlN FBAR, the maximum loaded quality factor Q_{max} is 614, fairly high in the X-band. For the epi-FBARs operating in the 1–6 GHz window, the figure of merit $f \cdot Q$ and $k_{eff}^2 \cdot Q$ are among 2–8 THz and 10-230 separately.[15–19,21,22] The figure of merit $f \cdot Q$ for the 9.2 GHz epi-FBAR in this paper is 5.6 THz, which is

reasonably high for an epi-AlN FBAR in the X-band (8–12 GHz). $k_{eff}^2 \cdot Q$ of the 9.2 GHz epi-FBAR is 8, which is low. More effort for the X-band epi-AlN FBARs is needed to realize a cleaner and stronger resonance as well as a higher electromechanical coupling coefficient.

The de-embedded data represent the intrinsic resonator part as well as a electrically conductive air pocket under the AlN layer, after removing the external circuit elements, such as the grounded coplanar waveguide (GCPW) stubs. Based on the de-embedded data, elements of the modified Butterworth–Van Dyke model (mBVD) were extracted,[35] as shown in Fig. 6(d). The mBVD model includes one R_0–C_0 branch (intrinsic properties of the capacitor-like acoustic resonator), one R_1–L_1–C_1 branch (a motional branch due to a piezoelectric effect) parallel to the intrinsic R_0–C_0 branch, and a L_X–R_X branch (associated with the electrodes of FBAR and a metallized air pocket) connected in series with the previous parallel sets. The de-embedded measured impedance data and modeled data fit well, as shown in Figs. 6(a)–6(c).

In addition to the primary mode characteristics, ripples were observed both in magnitude and phase plots of Z_{11}. These ripples exhibit a period of ≈0.1 GHz. The energy losses related to the FBAR scale can be divided into lateral loss and vertical loss. The lateral standing waves are likely responsible for the ripples in the impedance plot.[1] Adding a framed electrode or a border ring is able to help suppress the spurious modes. Extra modes due to the border ring should be avoided.[1] Another possible reason for the ripples is the non-uniform AlN film thickness after SiC TSV etching. To better understand the ripples, a focused ion beam (FIB) cut was performed on an FBAR active region to outline the cross-sectional morphology of the device.

As shown in Fig. 7(a), after SiC etching, the bottom of TSV etched into AlN has a tapered shape. The measured center AlN thickness is 350 nm, while at the edge of TSV, the AlN thickness is 420 nm. The detailed FBAR cross-sectional schematic is shown in Fig. 7(b). By reproducing Fig. 7(b) in a COMSOL multiphysics platform, the impedance characteristic Z_{11} was simulated, as shown in Fig. 7(c). The simulation reproduced the RF results of the fabricated FBAR, including $f_s \approx 9.17$ GHz (experimental result: 9.17 GHz), $f_p \approx 9.29$ GHz (experimental result: 9.23 GHz) as well
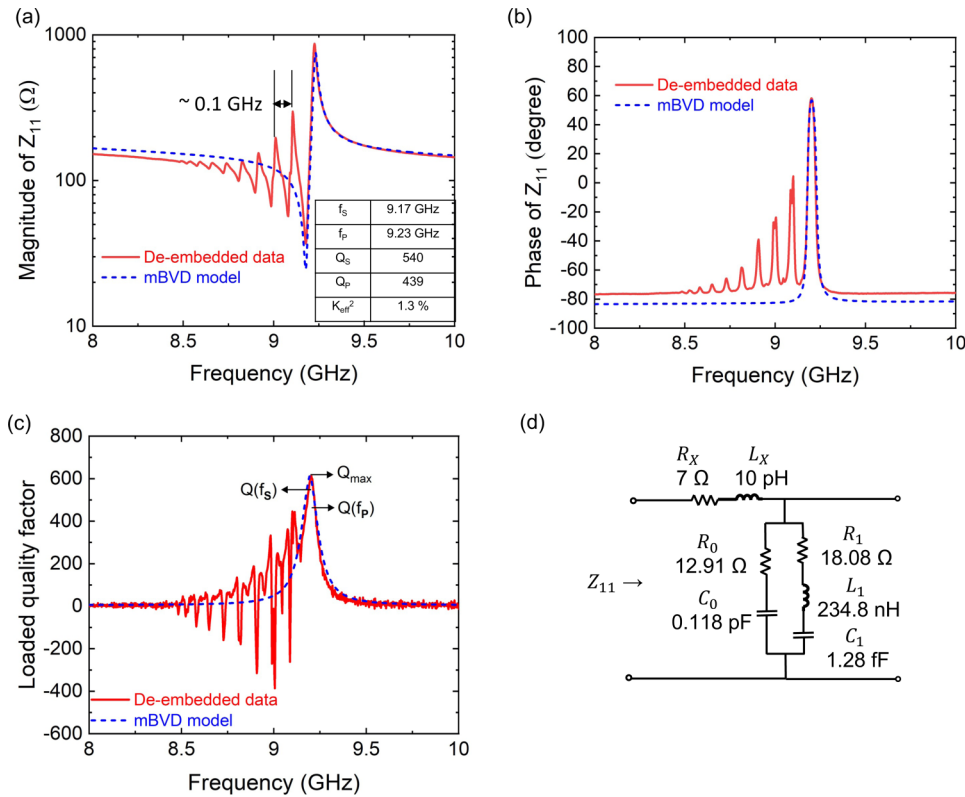
FIG. 6. (a) Magnitude plot and (b) the phase plot of Z_{11} of a loaded two-port shunt AlN FBAR in Fig. 5. (c) Loaded quality factor plot of the AlN FBAR in (a) and (b) driven by a 50-Ω source. (d) Modified Butterworth–Van Dyke (mBVD) model of the AlN FBAR in (a)–(c).

as the ripples with a period of 0.1 GHz. Based on $f = v_s/2L$, an estimate of the frequency shift due to the nonuniform AlN is $\Delta f \approx \frac{-v_s}{2 \cdot L^2} \cdot \Delta L$. For a 10 GHz signal, roughly a 3 nm thickness difference in the center of AlN will induce fairly strong ripples with a 0.1 GHz period. To validate that the ripples are due to nonuniform AlN, a calculation with a uniform AlN layer was performed, as shown in Fig. 7(d). In this model, except for the uniform thick AlN film, all other parameters are the same as those of the model with a nonuniform AlN in Fig. 7(c). In Fig. 7(d), a pure and strong fundamental resonance mode around 9.2 GHz is evaluated without ripples. The FBAR's electromechanical coupling coefficient k_{eff}^2, given by $k_{eff}^2 = \frac{\pi}{2} \cdot \frac{f_s}{f_p} \cdot \cot\left(\frac{\pi}{2} \cdot \frac{f_s}{f_p}\right)$, is a measure of the efficiency of energy conversion from the electromagnetic domain to the acoustic domain.[1] Higher k_{eff}^2 is expected in Fig. 7(d) at the expense of a quality factor. The COMSOL models shown in Figs. 7(c) and 7(d) suggest quantitatively that the observed ripples are because of the nonuniform AlN after the TSV etching.

IV. DISCUSSION AND CONCLUSIONS

The simulation in Fig. 7 indicates that the ripples lower the energy coupling and resonance strength of the primary resonance mode, consistent with the experimental result. The measured k_{eff}^2 of the FBAR (Fig. 6) is 1.3%, which is lower than the expected k_{eff}^2 of 6%–7% of the epi-AlN FBARs. An over-etching experiment was performed to confirm this hypothesis. For the 9.17 GHz FBAR, the equivalent AlN thickness is 350 nm. By further etching the AlN to 300 nm thickness, a higher frequency FBAR was fabricated, with $f_s \approx 10.49$ GHz, $f_p \approx 10.53$ GHz, $Q_s \approx 350$, and $Q_p \approx 176$. In this case, more ripples were observed to appear around the series resonance. The measured k_{eff}^2 was lowered to 0.93%. The resistance at parallel resonance R_p was measured to be 180 Ω, 30% of the R_p of the 9.2-GHz FBAR. With a similar resistance at series resonance R_s of 20–30 Ω, much lower R_p of the 10.5-GHz FBAR indicates a decreased resonance strength.

In order to reduce the ripples and increase k_{eff}^2, TSVs with a flatter bottom are needed. The flat TSV bottom can be realized using higher RIE power during SiC etching in the future. In addition to the uniformity of a piezoelectric layer, k_{eff}^2 depends on the electromechanical coupling coefficient k^2 of the piezoelectric, the acoustic impedance of electrodes, as well as the thickness ratio (t_E/t_P) of the electrode layer (t_E) over the piezoelectric layer (t_P). Highly crystalline AlN (002) films with a low full width at half maximum (FWHM) of the x-ray diffraction rocking curve exhibits k^2 as high as 8%.[1] Electrode metals with high acoustic impedance, such as Mo, W, and Ru, are choices to improve k_{eff}^2 of FBARs.[10] AlN FBARs utilizing Ru, Pt, Mo, W, Al, Ni, Au, or Cu as electrodes, with the t_E/t_P of 5%–10%, exhibit achievable high k_{eff}^2.[1] Epi-AlN FBARs can exhibit high k_{eff}^2 between 6% and 8%, with high quality piezoelectric films and careful design of the electrodes.
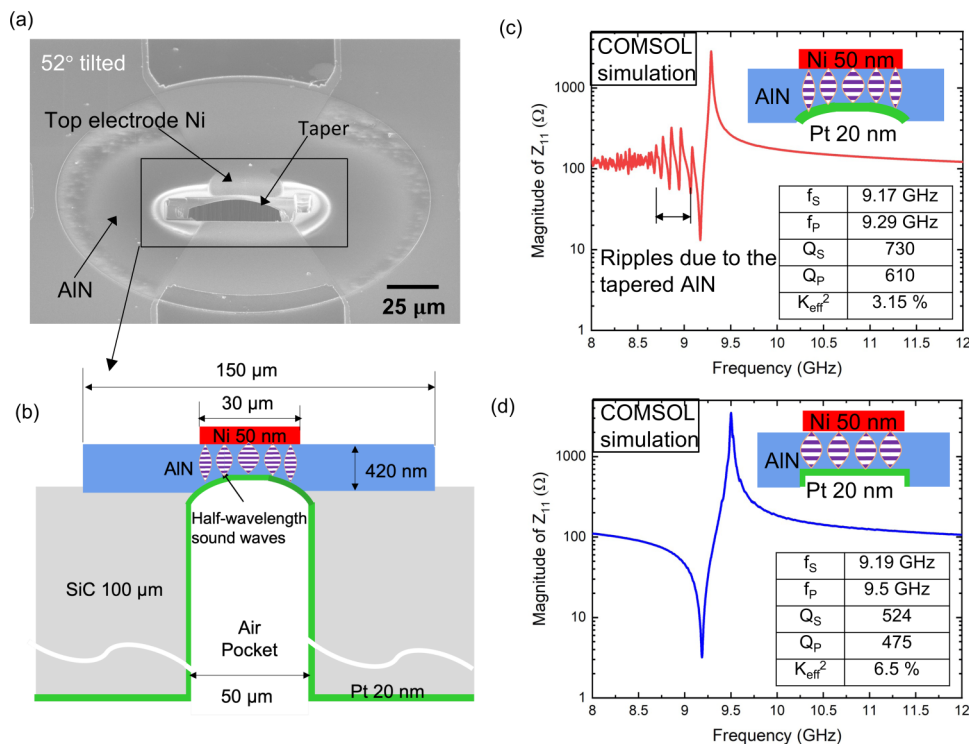
FIG. 7. (a) 52° tilted SEM figure showing the cross section of AlN FBAR. (b) The cross-sectional schematic in (a), showing a top electrode Ni, a non-uniform AlN layer, a backside electrode Pt as well as the air pocket underneath AlN FBAR. (c) COMSOL simulation of FBAR with non-uniform AlN (center thickness 350 nm). (d) COMSOL simulation of FBAR with a uniform AlN layer with a thickness of 350 nm.

The quality factor $Q = \frac{\omega}{2} \cdot \frac{E_{tot}}{\Delta P}$ quantifies the degree of damping of the oscillations. Here, E_{tot} is the total energy and ΔP is the power lost per half-cycle at frequency ω. Q values of 1000–4000 are typical for AlN FBARs operating in the frequency window of 1–5 GHz, where the AlN thickness L is 0.5–2 μm.[36] The power loss mechanisms are categorized into electrical loss, acoustic attenuation, and acoustic leakage. In the epi-BAWs reported here, the electrical losses dominate, followed by acoustic wave attenuation. For high quality factors in the X-band, FBARs need bottom electrodes, such as Al and Ru, with high electrical conductivity and high acoustic impedance to reduce the electrical and acoustic loss. Acoustic wave losses can be reduced using framed electrode geometries.[1]

In conclusion, using highly crystalline AlN piezoelectric thin films grown by MBE on SiC substrates, FBARs with a first-order thickness-extensional resonance mode at 9.2 GHz are demonstrated. Resonators fabricated on the same wafers using through-SiC vias and ALD metallization show consistent resonance frequencies and a Q_{max} of 614. For these epi-FBARs, undesired resonances can be eliminated with an AlN film of a uniform thickness after SiC via etching. TSVs with a more uniform and conductive metal coverage will enable FBARs with a lower loss and a higher quality factor. Such AlN-based FBARs provide a unique opportunity to be integrated with nitride HEMTs for RF applications and also with superconductors for microwave qubits for quantum computing. Importantly, such epi-BAW structure offers an opportunity for scaling microwave filters at higher frequencies than what are possible today, which is necessary for future communication systems.

AUTHOR DECLARATIONS

Conflict of Interest

The authors have no conflicts to disclose.

Author Contributions

Wenwen Zhao: Investigation (lead); Writing – original draft (lead). **Mohammad Javad Asadi:** Investigation (equal). **Lei Li:** Investigation (equal). **Reet Chaudhuri:** Investigation (equal). **Kazuki Nomoto:** Investigation (supporting). **Huili Grace Xing:** Funding acquisition (equal); Supervision (equal). **James C. M. Hwang:** Funding acquisition (equal); Supervision (equal). **Debdeep Jena:** Funding acquisition (equal); Supervision (equal); Writing – review and editing (equal).

DATA AVAILABILITY

The data that support the findings of this study are available from the corresponding author upon reasonable request.

REFERENCES

[1]K. Hashimoto, *RF Bulk Acoustic Wave Filters for Communications*, Artech House Microwave Library (Artech House, 2009).

[2]G. Chen and M. Rinaldi, J. Microelectromech. Syst. **29**, 148 (2020).

[3]Y. Yoshino, J. Appl. Phys. **105**, 061623 (2009).

[4]D. Bell and R. Li, Proc. IEEE **64**, 711 (1976).

[5]K. Umeda, H. Kawamura, M. Takeuchi, and Y. Yoshino, Vacuum **83**, 672 (2008).

[6]V. V. Felmetsger, P. N. Laptev, and R. J. Graham, J. Vac. Sci. Technol. A **29**, 021014 (2011).

[7]Y. Takagaki, P. V. Santos, E. Wiebicke, O. Brandt, H.-P. Schönherr, and K. H. Ploog, Appl. Phys. Lett. **81**, 2538 (2002).

[8]C. Xiong, X. Sun, K. Y. Fong, and H. X. Tang, Appl. Phys. Lett. **100**, 171111 (2012).

[9]M. Rinaldi, C. Zuniga, C. Zuo, and G. Piazza, in *TRANSDUCERS 2009—2009 International Solid-State Sensors, Actuators and Microsystems Conference* (IEEE, 2009), pp. 577–580.

[10]R. Ruby, in *2007 IEEE Ultrasonics Symposium Proceedings* (IEEE, 2007), pp. 1029–1040.

[11]H. W. Then, S. Dasgupta, M. Radosavljevic, P. Agababov, I. Ban, R. Bristol, M. Chandhok, S. Chouksey, B. Holybee, C. Y. Huang, B. Krist, K. Jun, K. Lin, N. Nidhi, T. Michaelos, B. Mueller, R. Paul, J. Peck, W. Rachmady, D. Staines, T. Talukdar, N. Thomas, T. Tronic, P. Fischer, and W. Hafez, in *2019 IEEE International Electron Devices Meeting (IEDM)* (IEEE, 2019), pp. 17.3.1–17.3.4.

[12]M. Akiyama, K. Umeda, A. Honda, and T. Nagase, Appl. Phys. Lett. **102**, 021915 (2013).

[13]D. Mo, S. Dabas, S. Rassay, and R. Tabrizian, "Complementary-switchable dual-mode SHF scandium-aluminum nitride BAW resonator," arXiv.2205.03446 (2022).

[14]D. Jena, R. Page, J. Casamento, P. Dang, J. Singhal, Z. Zhang, J. Wright, G. Khalsa, Y. Cho, and H. G. Xing, Jpn. J. Appl. Phys. **58**, SC0801 (2019).

[15]J. B. Shealy, R. Vetury, S. R. Gibb, M. D. Hodge, P. Patel, M. A. McLain, A. Y. Feldman, M. D. Boomgarden, M. P. Lewis, B. Hosse, and R. Holden, in *2017 IEEE MTT-S International Microwave Symposium (IMS)* (IEEE, 2017), pp. 1476–1479.

[16]M. D. Hodge, R. Vetury, S. R. Gibb, M. Winters, P. Patel, M. A. McLain, Y. Shen, D. H. Kim, J. Jech, K. Fallon, R. Houlden, D. M. Aichele, and J. B. Shealy, in *2017 IEEE International Electron Devices Meeting (IEDM)* (IEEE, 2017), pp. 25.6.1–25.6.4.

[17]R. Vetury, M. D. Hodge, and J. B. Shealy, in *2018 IEEE International Ultrasonics Symposium (IUS)* (IEEE, 2018), pp. 206–212.

[18]S. V. Krishnaswamy, J. D. Adam, and M. Aumer, in *2006 IEEE Ultrasonics Symposium* (IEEE, 2006), pp. 1467–1470.

[19]Y. Aota, Y. Sakyu, S. Tanifuji, H. Oguma, S. Kameda, H. Nakase, T. Takagi, and K. Tsubouchi, in *2006 IEEE Ultrasonics Symposium* (IEEE, 2006), pp. 337–340.

[20]A. Muller, D. Neculoiu, G. Konstantinidis, A. Stavrinidis, D. Vasilache, A. Cismaru, M. Danila, M. Dragoman, G. Deligeorgis, and K. Tsagaraki, IEEE Electron Device Lett. **30**, 799 (2009).

[21]J. B. Shealy, M. D. Hodge, P. Patel, R. Vetury, A. Y. Feldman, S. R. Gibb, M. D. Boomgarden, M. P. Lewis, J. B. Shealy, and J. R. Shealy, in *2016 IEEE Radio Frequency Integrated Circuits Symposium (RFIC)* (IEEE, 2016), pp. 103–106.

[22]M. Park, J. Wang, R. Dargis, A. Clark, and A. Ansari, in *2019 IEEE International Ultrasonics Symposium (IUS)* (IEEE, 2019), pp. 1689–1692.

[23]V. J. Gokhale, B. P. Downey, D. S. Katzer, L. B. Ruppalt, and D. J. Meyer, in *2019 IEEE International Electron Devices Meeting (IEDM)* (IEEE, 2019), pp. 17.5.1–17.5.4.

[24]L. C. Popa and D. Weinstein, in *Solid-State Sensors, Actuators, and Microsystems Workshop, Hilton Head Island, SC, 5–9 June 2022* (IEEE, 2014), pp. 8–12.

[25]A. Ansari and M. Rais-Zadeh, "An 8.7 GHz GaN micromechanical resonator with an integrated AlGaN/GaN HEMT," in *Proceedings Hilton Head Workshop* (MDPI, 2014), pp. 295–296.

[26]A. Hickman, R. Chaudhuri, L. Li, K. Nomoto, S. J. Bader, J. C. M. Hwang, H. G. Xing, and D. Jena, IEEE J. Electron Devices Soc. **9**, 121 (2021).

[27]A. Hickman, R. Chaudhuri, S. J. Bader, K. Nomoto, K. Lee, H. G. Xing, and D. Jena, IEEE Electron Device Lett. **40**, 1293 (2019).

[28]A. L. Hickman, R. Chaudhuri, S. J. Bader, K. Nomoto, L. Li, J. C. M. Hwang, H. G. Xing, and D. Jena, Semicond. Sci. Technol. **36**, 044001 (2021).

[29]N. Nguyen, A. Johannessen, S. Rooth, and U. Hanke, Ultrasonics **94**, 92 (2019).

[30]R. Tabrizian, M. Rais-Zadeh, and F. Ayazi, in *TRANSDUCERS 2009—2009 International Solid-State Sensors, Actuators and Microsystems Conference* (IEEE, 2009), pp. 2131–2134.

[31]R. Y. Vidana Morales, S. Ortega Cisneros, J. R. Camacho Perez, F. Sandoval Ibarra, and R. Casas Carrillo, Sensors **21**, 2715 (2021).

[32]M. J. Asadi, L. Li, W. Zhao, K. Nomoto, P. Fay, H. G. Xing, D. Jena, and J. C. M. Hwang, in *2021 IEEE MTT-S International Microwave Symposium (IMS)* (IEEE, 2021), pp. 669–672.

[33]M. Qi, G. Li, V. Protasenko, P. Zhao, J. Verma, B. Song, S. Ganguly, M. Zhu, Z. Hu, X. Yan, A. Mintairov, H. G. Xing, and D. Jena, Appl. Phys. Lett. **106**, 041906 (2015).

[34]D. A. Feld, R. Parker, R. Ruby, P. Bradley, and S. Dong, in *2008 IEEE Ultrasonics Symposium* (IEEE, 2008), pp. 431–436.

[35]J. Larson, P. Bradley, S. Wartenberg, and R. Ruby, in *2000 IEEE Ultrasonics Symposium. Proceedings. An International Symposium (Cat. No. 00CH37121)* (IEEE, 2000), Vol. 1, pp. 863–868.

[36]Y. Liu, Y. Cai, Y. Zhang, A. Tovstopyat, S. Liu, and C. Sun, Micromachines **11**, 630 (2020).